Using Anatomical Knowledge Expressed as Fuzzy Constraints to Segment the Heart in CT Images

A. Moreno [a,b] C.M. Takemura [a] O. Colliot [c] O. Camara [d]
I. Bloch [a]

[a] *Ecole Nationale Supérieure des Télécommunications (GET - Télécom Paris), CNRS UMR 5141 LTCI - Signal and Image Processing Department, 46 rue Barrault, 75634, Paris Cedex 13, France*

[b] *Segami Corporation, Paris, France*

[c] *Cognitive Neuroscience and Brain Imaging Laboratory, CNRS UPR 640-LENA, Université Pierre et Marie Curie – Paris 6, Hôpital de la Pitié-Salpêtrière, Paris, France*

[d] *Center for Medical Image Computing, Dept. of Medical Physics, University College London, London WC1E 6BT, UK*

Abstract

Segmenting the heart in medical images is a challenging and important task for many applications. In particular, segmenting the heart in CT images is very useful for cardiology and oncological applications such as radiotherapy. Although the majority of methods in the literature are designed for ventricle segmentation, there is a real interest in segmenting the heart as a whole in this modality. In this paper, we address this problem and propose an automatic and robust method, based on anatomical knowledge about the heart, in particular its position with respect to the lungs. This knowledge is represented in a fuzzy formalism and it is used both to define a region of interest and to drive the evolution of a deformable model in order to segment the heart inside this region. The proposed method has been applied on non-contrast CT images and the obtained results have been compared to manual segmentations of the heart, showing the good accuracy and high robustness of our approach.

Key words: Heart segmentation, spatial relations, anatomical knowledge, deformable models, fuzzy logic, CT.

Email address: Antonio.Moreno@enst.fr (A. Moreno).

1 Introduction

Segmenting the heart in medical images such as non-contrast computed tomography (CT) images is a challenging task because of their low contrast and the similar grey-level values of the surrounding structures. Many clinical applications could benefit from a reliable heart segmentation procedure, such as the study of cancer in the thoracic region or other cardiac and vascular diseases. The delineation of the heart is important in oncological applications such as dose estimation in radiotherapy. The segmentation of the heart may be used in treatment planning in order to define a security margin around this organ to prevent it from being irradiated: usually radiotherapists delineate a relatively wide margin around sensitive organs which must not be affected by radiation. This margin may be of several centimeters (particularly in the lungs due to the breathing). Heart segmentation can also be useful as a preliminary step for registration of multimodality images, such as CT, positron emission tomography (PET), single photon emission computed tomography (SPECT) or magnetic resonance imaging (MRI), and in particular for those obtained with new combined PET/CT or SPECT/CT devices.

1.1 Related work

Most heart segmentation methods proposed in the literature deal with the segmentation of internal structures (in particular the left ventricle) as in [1–7] for instance. However, there is also a need to segment the heart as a whole in order to distinguish its limits and the separations with surrounding structures such as the liver or the aorta. The existing methods for segmenting the heart have been focused on MRI modality [5,7–11] or ultrasound [6,12] but rarely on CT [13–16]. However, for the aforementioned applications, CT is one of the most common anatomical imaging modalities.

Numerous cardiac segmentation methods have been developed to estimate the myocardial boundaries in MR images. A registration-based model is used in [5] and a clustering technique in [7]. Some methods [10,11] use prior knowledge learned from images models. Deformable models have also been widely used in segmenting cardiac images [11]. However, all these approaches rely on models obtained from MR images, on the modality acquisition (intensity values) or on the structures visible in this modality, in particular, the left ventricle. Therefore, they are not adapted to our problem on CT images.

Among the existing methods for segmenting the heart as a whole, Gregson [8] works on MR images where he manually selects a 2D slice containing the heart and then uses a hierarchical algorithm to segment other structures in this slice

(torso, lungs, background). Once the heart is recognized in the selected slice, the segmentation is propagated to adjacent slices. Lelieveldt et al. [9] proposed another method to segment the heart as a whole in MR images. They base their segmentation on a fuzzy atlas of thoracic structures. Their method is applied on MR data and the fuzzy model must be built beforehand, which is a strong limitation, in particular for the segmentation of pathological images that may have a different structural configuration than the ones used for the atlas construction.

The segmentation method proposed by Jolly [14] was first developed to segment the left ventricle in 2D MR slices, and it has been extended to CT with minimal adjustments. Her method proceeds in two steps. First, a global localization step roughly localizes the left ventricle and then a local deformation step combines EM-based (Expectation-Maximization) region segmentation and Dijkstra active contours. One of the main difficulties she has found is that the epicardium is difficult to recover because there are no image edges between the myocardium and the liver. This method furnishes very satisfactory results for high-resolution contrast CT images. However, it is not directly applicable to non-contrast and low resolution 3D CT images and major adaptations and extensions would be needed.

The work by Funka-Lea et al. [13] deals with the segmentation of the heart as a whole in CT. Their goal is to isolate the outer surface of the entire heart in order to easily visualize the coronary vessels. They make use of graph-cuts for the segmentation [17,18]. Their method is fast and robust for contrast CT studies with sub-millimeter resolution where the brightest regions are bone and blood. However, as the initialization of the graph-cut algorithm depends on the characteristics of a contrast study, it is not adapted to non-contrast CT images, which are common in radiotherapy applications. The goal and the type of images are therefore different from the ones in the present application.

The work by Ecabert et al. [15,16] describes a multi-compartment mesh of both atria, both ventricles, the myocardium around the left ventricle and the trunks of the great vessels and it is adapted to an image volume. The adaptation is performed in a coarse-to-fine manner by progressively relaxing constraints on the degrees of freedom of the allowed deformations. Their method is largely validated on high resolution contrast CT and it furnishes very satisfactory results.

However, these methods are not directly applicable to non-contrast and low resolution 3D CT images and major adaptations and extensions would be needed. The segmentation of the heart in non-contrast CT images presents specific difficulties due to their low contrast and the similar grey-level values of the surrounding structures (liver, tumors). This is illustrated in Figure 1 where it can be observed that the limits between the heart and the aorta or the

liver are difficult to distinguish visually (even for experts). The low resolution (compared to existing submillimetric CT data) and the anisotropy of these CT exams are additional difficulties for the segmentation of the heart. Due to these difficulties, non-contrast CT is not generally used in cardiology. Other non irradiant techniques such as ultrasounds, which are less invasive, or MRI, which can provide a better resolution and contrast, are usually preferred in this field. However, ultrasounds do not furnish enough quality for many applications and MRI is not yet a routine technique in many medical centers. In the case of using CT for cardiac applications, contrast CT exams are acquired. For these reasons, to the best of our knowledge, there exists no method for the segmentation of the heart for non-contrast CT images and the existing methods for other modalities cannot deal with this type of images. Even the methods applied on CT images cannot be used on non-contrast studies without previous adaptation. Non-contrast CT is widely used in clinical routine and additionally provides better quality for the study of hard tissues such as bones, which can serve as a rigid references for several applications such as registration, surgery or radiotherapy planning. For oncology and radiotherapy, heart segmentation is very useful and the processing of this modality would avoid the necessity of other supplementary imaging acquisitions.

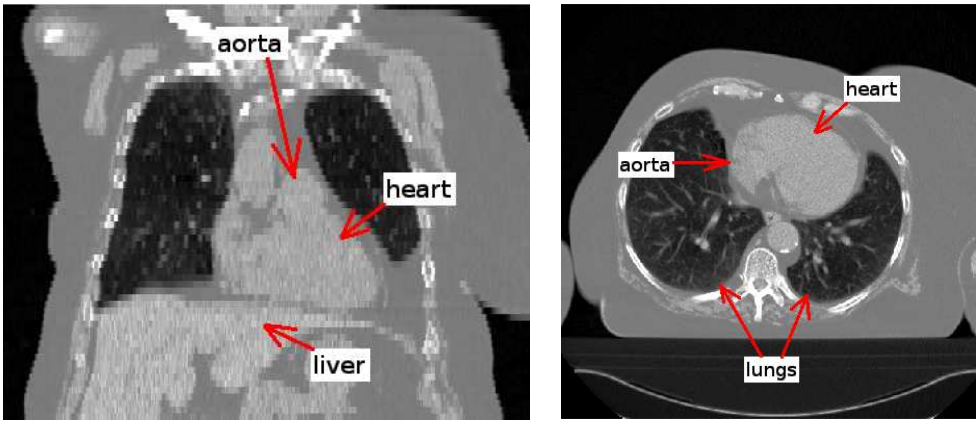

Fig. 1. Coronal (left) and axial (right) views of a CT image.

1.2 Overview of the proposed method

In spite of the aforementioned drawbacks of the CT images used in radiotherapy, they have some particular characteristics, as the homogeneity of morphologic structures signal and the high contrast of the lungs compared to their surrounding structures. Therefore, we propose an original method that relies on these particular features of the images. The proposed algorithm includes constraints and anatomical knowledge in order to perform a robust segmentation of the heart by guiding a deformable model and thus, overcome the limits

of the image acquisition.

Our approach relies on the segmentation of neighboring structures, which provide a strong constraint on the relative position and shape of the targeted structure. Based on the same principle, we have developed hierarchical methods to segment different organs of the body such as deep brain structures [19] or thoracic and abdominal structures [20]. The idea is to deal first with the easiest structures to segment and then continue with those of increasing difficulty, using prior knowledge about the position of a structure with respect to the previously segmented ones. As shown in [21,22], spatial relations improve the robustness of the segmentation of the structures even in the presence of pathologies. Another class of methods segment multiple objects simultaneously. For example, a level set approach based on a maximum a posteriori (MAP) framework using a neighbor prior constraint is used in [23].

In this paper, we propose an automatic method to segment the heart as a whole based on the modeling of spatial relations between the heart and the lungs. Since the segmentation of the lungs is generally simple in CT scans due to their high contrast with respect to surrounding tissues, they are segmented first in order to define a region of interest (ROI) of the heart. This region is used to define the initialization of a deformable model. Then the anatomical knowledge is included in the deformable model to segment the heart. A preliminary version of our method can be found in [24], where the use of the spatial relation "between" is explored in order to segment the heart. This study has shown encouraging results. In this paper a deeper study is developed, new pieces of anatomical knowledge are taken into account to improve the robustness and the automaticity of our approach, and the method is applied on a larger database.

In Section 2, our approach based on anatomical knowledge representation is introduced. In Section 3, we describe the first step of our method which defines the region of interest of the heart. Then in Section 4 the segmentation of the heart using deformable models constrained by anatomical knowledge is described. Next, in Section 5 some results are shown and compared with manual segmentations.

2 Expression of anatomical knowledge

Although the delineation of the heart is a difficult task in CT, experts are able to segment this organ manually because they rely on their expertise and their knowledge of the anatomy. This a priori knowledge is usually represented by anatomical descriptions using qualitative and imprecise statements. Translating this type of knowledge in a computationally efficient form, suitable for

image processing, requires to model mathematically vague statements and imprecision. Therefore, a fuzzy representation of this kind of knowledge fulfills our requirements.

The anatomical descriptions of the heart usually include the statement "the heart is between the lungs". Our method relies on modeling this statement (denoted by K1) as well as the position of the heart (K2 and K3) inside this region:

- K1: "the heart is between the lungs".
- K2: the center of the heart is "between the lungs and far from them (i.e. the center of the heart is in the middle of the lungs in the region which is the furthest from both lungs) but closer to the left lung than to the right lung".
- K3: the heart is placed "in the anterior (closer to the chest than to the back) and inferior (near the diaphragm) region of the bounding box of the lungs".

The preliminary step consists in segmenting the lungs. This is done using a method inspired from [20] and relies on the following steps. First, a classification using the k-means algorithm is used in order to detect the lungs. Then, a consistency test is applied in order to verify that the volume of the segmented lungs has a plausible value. If it is the case, the result is refined by using some mathematical morphology operations (a hole filling and a closing) and a deformable model in which the GVF (Gradient Vector Flow) [25] is used as a term of fidelity to the data. Otherwise, the process is repeated with another class in the k-means algorithm. An example of the segmentation of the lungs is illustrated in Figure 2(a).

2.1 Modeling K1

A complete study of the spatial relation "between" has been made in [26], in which different definitions of this spatial relation are proposed, compared and discussed according to different types of situations.

A simple (crisp) definition of "between" consists in using the convex hull of the union of the two involved objects. However, the use of a convex hull to find the heart is not suitable because some parts of the organ are outside the resulting region as illustrated in Figure 2. This is a strong argument in favor of more sophisticated definitions which should take into account a larger region than the convex hull corresponding to a somewhat looser meaning of the "between" area.

This idea is achieved by means of fuzzy dilation of each object in the direction of the other. Thus, among the definitions detailed in [26], we have chosen the

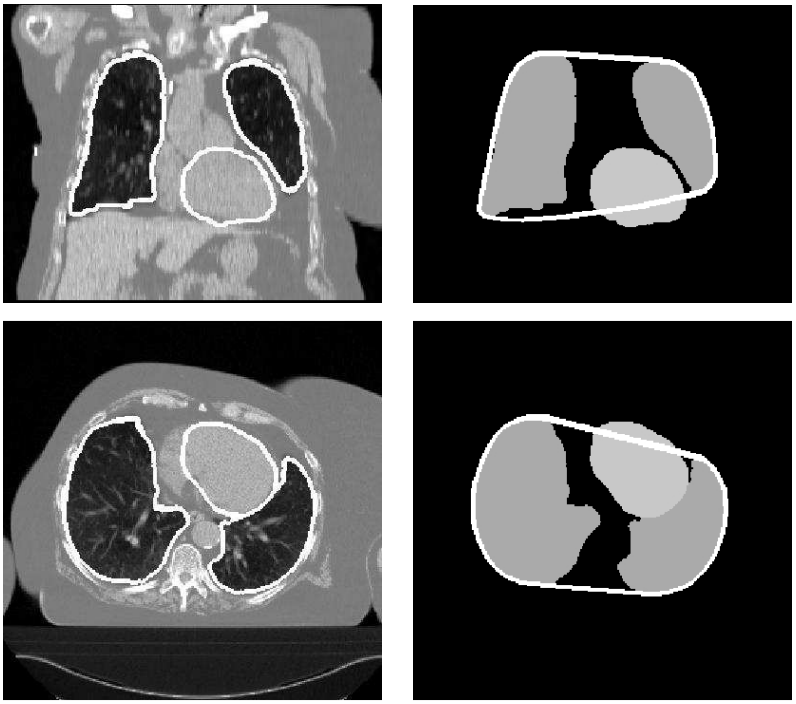

(a) (b)

Fig. 2. Coronal (top row) and axial (bottom row) views of an example of the segmentation of the lungs and the heart: (a) the contours of these organs are superimposed on the original image and (b) the convex hull of the lungs is superimposed on the segmented lungs and heart (some parts of the heart are not contained in this region).

fuzzy directional dilation definition of the relation "between". The interest of this definition is that the "between" region extends smoothly outside the convex hull of the union of both objects which is a required feature for our application. The region between A_1 and A_2 is defined as a fuzzy set in the image domain, as:

$$\begin{aligned}\beta_{btw}(A_1, A_2) = D_{\nu_2}(A_1) \cap D_{\nu_1}(A_2) \cap A_1^C \cap A_2^C \\ \cap [D_{\nu_1}(A_1) \cap D_{\nu_1}(A_2)]^C \cap [D_{\nu_2}(A_1) \cap D_{\nu_2}(A_2)]^C\end{aligned} \tag{1}$$

where A_1 and A_2 represent the objects (the lungs in our case), A^C represents the (fuzzy) complementation of A and $D_{\nu_i}(A_j)$, $i, j \in \{1, 2\}$, is the fuzzy dilation of A_j with the fuzzy structuring element ν_i as defined in [27]:

$$D_\nu(\mu)(x) = \sup_y t[\mu(y), \nu(x - y)]. \tag{2}$$

Thus, fuzzy dilation corresponds to a degree of intersection between the fuzzy set to be dilated μ and the fuzzy structuring element ν translated at point x. t denotes a t-norm and x and y points of space. An example of fuzzy dilation is

shown in Figure 3(d). The conjunctions ($\cap$) in Equation 1 are performed using the t-norm "minimum". The membership degree $\beta_{btw}(A_1, A_2)(x)$ represents the degree to which x is between A_1 and A_2.

The structuring elements are derived from the angle histogram between both objects [28]. In 3D (using spherical coordinates) the direction is represented by two angles, that are denoted by α_1 and α_2 (with $\alpha_1 \in [0, 2\pi[$ and $\alpha_2 \in [-\pi/2, \pi/2]$, the 2D case corresponding to $\alpha_2 = 0$) [29]. Given an axis of reference, say the x axis denoted by $\vec{u}_x$, for each pair of points (p_1, p_2) with $p_1 \in A_1$ and $p_2 \in A_2$, the angles between the axis and the segment joining these two points, $\overrightarrow{p_1p_2}$, are computed: α_2 is the angle between $\overrightarrow{p_1p_2}$ and its projection on the x-y plane and α_1 is the angle between this projection and $\vec{u}_x$. The histogram of the obtained angles $h_{(A_1,A_2)}(\alpha_1, \alpha_2)$ for all possible pairs of points is then defined as:

$$h_{(A_1,A_2)}(\alpha_1, \alpha_2) = |\{(p_1, p_2), p_1 \in A_1, p_2 \in A_2, \angle(\overrightarrow{p_1p_2}, \vec{u}_x) = (\alpha_1, \alpha_2)\}|. \quad (3)$$

It can be normalized as:

$$H_{(A_1,A_2)}(\alpha_1, \alpha_2) = \frac{h_{(A_1,A_2)}(\alpha_1, \alpha_2)}{\max_{(\alpha'_1,\alpha'_2)} h_{(A_1,A_2)}(\alpha'_1, \alpha'_2)} \quad (4)$$

in order to be interpreted as a fuzzy set.

The structuring elements are derived as:

$$\nu_2(r, \alpha_1, \alpha_2) = H_{(A_1,A_2)}(\alpha_1, \alpha_2), \quad (5)$$

$$\begin{aligned} \nu_1(r, \alpha_1, \alpha_2) &= H_{(A_1,A_2)}((\alpha_1 + \pi)(\mathrm{mod}\, 2\pi), -\alpha_2) \\ &= \nu_2(r, (\alpha_1 + \pi)(\mathrm{mod}\, 2\pi), -\alpha_2), \end{aligned} \quad (6)$$

where r is the radius in spherical coordinates. The structuring elements represent the relation between the two objects and they define the direction to be used for the fuzzy dilation [30]. ν_1 represents the direction from object A_2 to object A_1 and ν_2 the opposite direction.

An illustrative example in 2D is shown in Figure 3 where A_1 (the right lung) is on the left in the figure and A_2 (the left lung) is on the right. For instance, if object A_2 is mainly to the right of object A_1 (in the figure) (see Figure 3(d)), then ν_1 represents "to the left of" and ν_2 "to the right of". Equation 1 defines the region which is both to the right of A_1 ($D_{\nu_2}(A_1)$) and to the left of A_2 ($D_{\nu_1}(A_2)$) excluding A_1 and A_2 ($A_1^C \cap A_2^C$), but which is not to the left of both A_1 and A_2 ($[D_{\nu_1}(A_1) \cap D_{\nu_1}(A_2)]^C$) nor to the right of both ($[D_{\nu_2}(A_1) \cap$

$D_{\nu_2}(A_2)]^C$). Figure 3(e) shows the region between the lungs obtained with this definition.

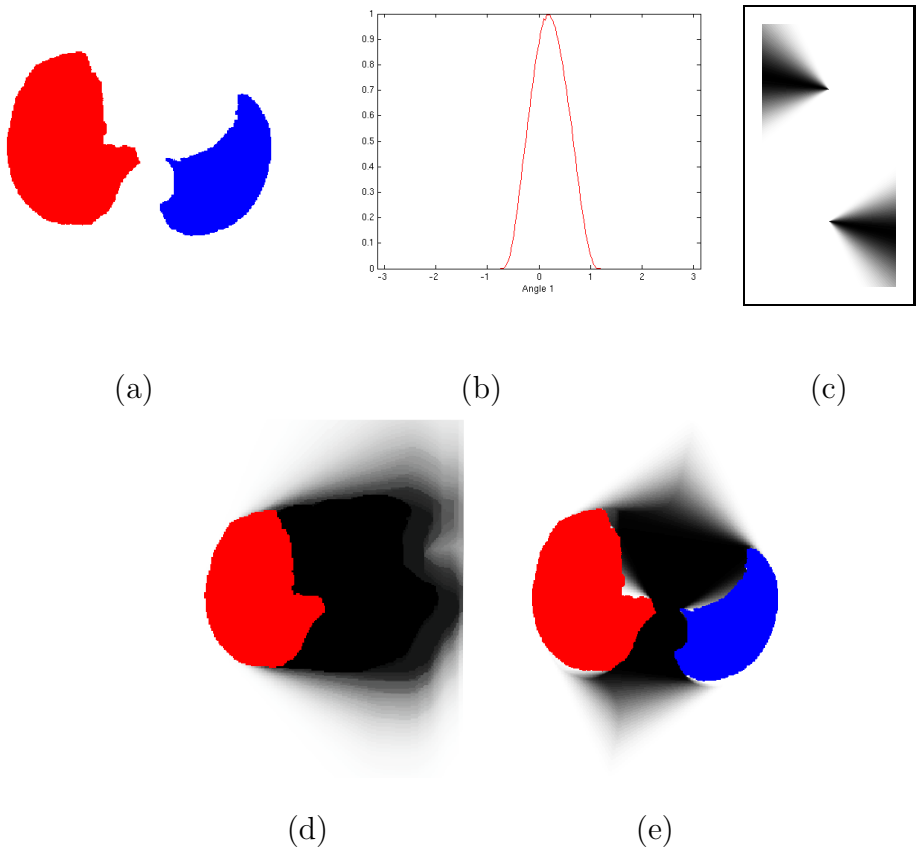

Fig. 3. Some of the steps for computing $\beta_{btw}(A_1, A_2)$: (a) The segmented lungs A_1 (in red) and A_2 (in blue), (b) the normalized angle histogram $H_{(A_1,A_2)}$ with respect to the horizontal axis, (c) the structuring elements ν_1 (top) and ν_2 (bottom), (d) fuzzy dilation of the right lung (A_1) with the fuzzy structuring element ν_2, $D_{\nu_2}(A_1)$, (e) fuzzy region β_{btw} between the lungs, superimposed on the segmented lungs. The membership values to β_{btw} vary from 0 (white) to 1 (black). The illustration is provided in 2D for the sake of readability.

An example of the region between the lungs obtained in 3D with this definition is shown in Figure 4(a).

2.2 Modeling K2

K2 represents the following anatomical knowledge: the center of the heart is "between the lungs and far from them (i.e. close to the middle of the lungs) but closer to the left lung than to the right lung". The computation of a distance function to the lungs combined with K1 allows the modeling of the first part

of this statement. In order to account for the second part, a dilated right lung has been used to calculate the distance function. Thus, the maximum of the distance function between the lungs is closer to the left lung. In order to find how much the center of the heart is closer to the left lung than to the right lung, some measures have been performed by an expert on images from different patients. In addition to this, the distances of the centroid of the heart (the center of its bounding box) have been computed for the 10 cases of our database where the heart has been manually segmented. The results in Table 1 confirm that the centroid of the heart is 2-3 cm closer to the left lung than to the right lung. For this reason, a morphological dilation of 3 cm for the right lung has been used to find correctly the approximate center of the heart. The distance function d is computed using a chamfer algorithm [31]. The normalized distance function can be interpreted as a fuzzy set which represents the region "far from the lungs but closer to the left lung". Therefore, its membership function β_{ffl}, illustrated in Figure 4(b), is defined at a point x as:

$$\beta_{ffl}(x) = \frac{d(x, D_3(A_1) \cup A_2)}{\max_y d(y, D_3(A_1) \cup A_2)}. \quad (7)$$

where $D_3(A_1)$ denotes the morphological dilation of 3 cm of the right lung and A_2 the left lung.

Distance of the heart centroid to the right lung (mm)	69.98 ± 7.96
Distance of the heart centroid to the left lung (mm)	47.35 ± 6.12
% of bounding box of lungs in y	31.7 ± 7.18
% of bounding box of lungs in z	32.1 ± 7.98

Table 1
Mean and standard deviation of the distances of the centroid of the heart to both lungs (for K2) and mean and standard deviation of the percentage of the bounding box of the lungs where the centroid of the heart is located (for K3).

2.3 Modeling K3

The heart is placed in the anterior (closer to the chest than to the back) and inferior (near the diaphragm) region of the bounding box of the lungs. Here it is assumed that the patients are always in a similar position and that the orientation does not change from one patient to another (there is almost no difference in rotation), and therefore the bounding boxes of the lungs are comparable. This region is defined as the inverted (normalized) distance β_{BB} to a horizontal line L which is at 1/3 (33 %) of the height of the bounding box

from its inferior limit and at 1/3 (33 %) of its width in the anterior-posterior direction from its anterior limit:

$$\beta_{BB}(x) = 1 - \frac{d(x, L)}{\max_y d(y, L)} \tag{8}$$

As for K2, the position of the horizontal line L was estimated by an expert on images from different patients and it has been confirmed by the results illustrated in Table 1 which shows the mean and standard deviation of the position of the centroid of the heart with respect to the bounding box of the lungs. The fuzzy set β_{BB} is illustrated in Figure 4(c) where it can be observed that the value of β_{BB} decreases linearly when the distance to L increases.

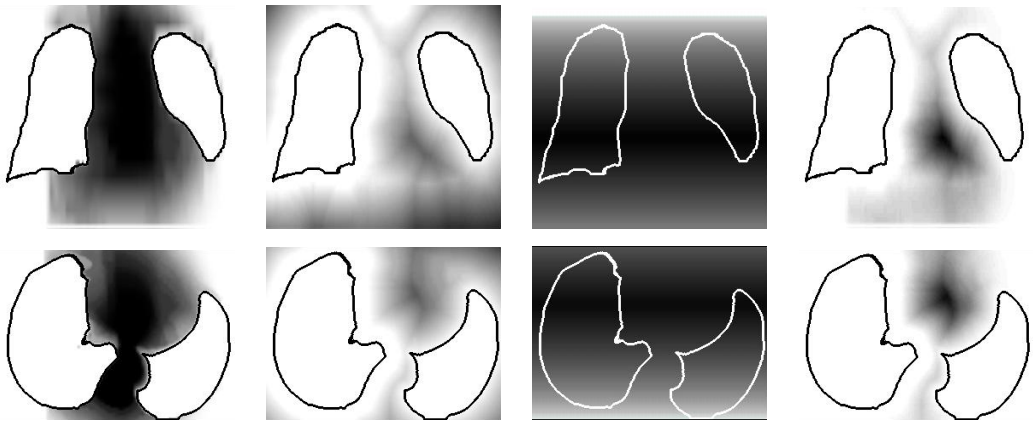

(a) (b) (c) (d)

Fig. 4. (a) K1, the spatial relation "between", β_{btw}, (b) K2, the distance map to the lungs, β_{ffl}, (c) K3, the distance map to the horizontal line, β_{BB}, and (d) conjunctive fusion of K1, K2 and K3, β_R. The membership values vary from 0 (white) to 1 (black). Coronal views are in the top row and axial views in the bottom one. The contours of the lungs are superimposed in black (a,b,d) and in white (c) for better visualization.

2.4 Using K1, K2 and K3

Although K2 and K3 are not as critical as K1, they have proved to be useful in order to get a robust and automatic initialization in all cases. If K1 is not included, anything but the heart can be segmented (typically, something in the abdomen if it is included in the image) because the processing is not centered in the region between the lungs. If K2 is not used, the aorta can be segmented instead of the heart, since it is between the lungs but not in the widest part between them. If K3 is not used, then some parts of the heart are not segmented but the aorta is included in the result of the segmentation since

it is located in the superior region of the lungs bounding box. Without K2 and K3, the algorithm furnishes an incomplete result or a result that includes too many structures. Thus the use of K2 and K3 improves the results by refining anatomical knowledge.

The exploitation of all this anatomical knowledge is performed at two levels:

(1) first a region of interest (ROI) is selected by combining the different pieces of anatomical knowledge (Section 3);
(2) then the anatomical knowledge is introduced in the evolution scheme of a deformable model to find the boundaries of the heart inside the ROI (Section 4).

3 Definition of the region of interest

The goal of the step described in this section is to find a ROI containing the heart which is defined as a sphere centered in a point obtained in a robust way using the anatomical knowledge modeled as stated in the previous section. In 2D, as explained by Gregson [8], the maximum of the distance function to the lungs (on a previously selected slice containing the heart) is a good candidate to be the center of a disk containing this organ. This uses only a part of K2 in 2D, which leads to a poor robustness in general. We propose to extend this idea to 3D and to improve the localization by using K1, K2 and K3. Thus, the algorithm to find the center of the ROI has the following steps:

(1) Conjunctive fusion of β_{btw}, β_{ffl} and β_{BB}:

$$\beta_R(x) = \beta_{btw}(A_1, A_2)(x) \cdot \beta_{ffl}(x) \cdot \beta_{BB}(x).$$

This conjunctive combination of K1, K2 and K3, realized with the t-norm "product", means that the points with higher values will fulfill all the spatial constraints. The result of this combination is illustrated in Figure 4(d).
(2) Calculation of the sphere-ROI. The center of the sphere is defined as the point having the maximum value in the fusion result. The radius is defined as the value of the minimum distance to the right lung at this point plus 10% of this distance (so that the relation is large enough to include the heart in all cases).

This stage provides a restricted ROI for the heart (not too many surrounding structures included) and it has proven to be robust enough since it uses some stable characteristics of the center of the heart and relies on general anatomical knowledge. This is illustrated in Figure 5, where the resulting ROIs for 5 cases are superimposed on the original CT images.

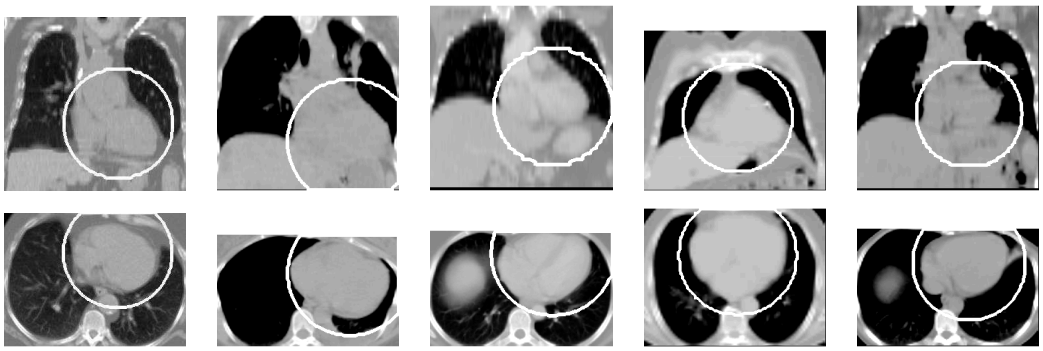

(a) (b) (c) (d) (e)

Fig. 5. Superimposition of the obtained ROIs (circles) and the original images for 5 cases. Coronal views are in the top row and axial views in the bottom one.

4 Deformable model with anatomical constraints

Once the region of interest is selected, a deformable model is used to segment the heart inside this region.

Deformable models were introduced by Kass et al. [32] and are often used for segmentation in image processing [33–37]. They consist in defining an initial m-D object in n-D, with $n \geq m$ (a 3D surface in 3D in the present case) that evolves under the effect of some forces towards a final state. In an optimal case, this final state corresponds to the object to be segmented.

The evolution of the deformable surface of negligible mass $\mathbf{X}$ can be described using a dynamic force formulation and written as follows:

$$\gamma \frac{\partial \mathbf{X}}{\partial t} = \mathbf{F}_{int}(\mathbf{X}) + \mathbf{F}_{ext}(\mathbf{X})$$

where $\mathbf{F}_{int}$ is the internal force related to the physical properties or constraints of the model that specifies the regularity of the surface, and $\mathbf{F}_{ext}$ is the external force that drives the surface towards the desired features in the image (in general image edges) and sometimes includes forces interactively introduced by the user. The solution is the steady state of the previous equation.

The internal force is defined as [32]:

$$\mathbf{F}_{int} = \alpha \, \nabla^2 \mathbf{X} - \beta \, \nabla^2 (\nabla^2 \mathbf{X}) \tag{9}$$

where α and β respectively control the surface tension (which prevents it from stretching) and rigidity (which prevents it from bending) and ∇^2 is the Laplacian operator.

The external force can be defined with the Gradient Vector Flow (GVF) [25] as also used in [20,19,38]. The GVF defines a vector field towards the previously calculated contours of the image (the edge map). As proposed in [39,38] the external force can also include spatial relations in order to constraint the segmented object to stay in a region where given spatial relations are satisfied.

The anatomical knowledge described in Section 2 is introduced in the external force $\mathbf{F}_{ext}$ combined with a weighted pressure force. Thus, the external force describes both edge information (GVF) and structural constraints:

$$\mathbf{F}_{ext} = \lambda\, \mathbf{F}_{gvf} + (1 - \lambda)\, \mathbf{F}_R + \mathbf{F}_p \tag{10}$$

where $\mathbf{F}_{gvf}$ is a classical data term that drives the model towards the edges [25], $\mathbf{F}_R$ is a force associated to the spatial relations, $\lambda \in [0, 1]$ is a weighting parameter and $\mathbf{F}_p$ represents a pressure force [40], normal to the surface.

4.1 Initialization of the deformable model

The initial surface is a sphere included in the ROI (same center) chosen small enough so that it can be assumed that it has to expand to segment correctly the heart. In this work, the size of the small sphere has been fixed to 10 mm, but it could also be defined as a percentage of the radius of the ROI. A small sphere has been chosen as initialization (instead of directly the sphere-ROI) in order to ease the evolution of the deformable model. If the sphere-ROI is used as initialization and deformed by enforcing contraction, the deformable model stops at the high contrast contours outside the heart and an erroneous segmentation would be obtained. However, inside the heart, there exist much less contrasted contours and thus the deformable model evolves towards the external limits of this organ. The initial small sphere is illustrated in Figure 6. During its evolution, the deformable model is constrained to remain inside the sphere-ROI. This can be seen as a restriction. However, the sphere-ROI is large enough to ensure that the heart is contained in it in all tested cases. If the center of the ROI has been computed correctly (i.e. it is in the center of the heart), the heart will be contained in the ROI.

4.2 Spatial relations force

The force $\mathbf{F}_R$ must constraint the model to evolve towards the regions with high values of $\beta'_R = 1 - \beta_R$. This means that the force $\mathbf{F}_R$ drives the deformable model towards regions closer to the lungs and "less between" them than the center, which is the complementary of K1, K2 and K3 defined in

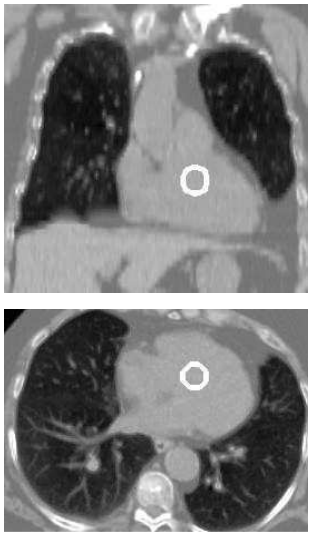

Fig. 6. Coronal and axial views of the obtained ROI of the heart and the initial contour of the deformable model superimposed on the CT image.

Section 2. When the relation β'_R is completely satisfied (inside the lungs and in the regions not between them), the model should only be driven by edge information ($\mathbf{F}_{gvf}$) and $\mathbf{F}_R$ should be 0 if $\beta'_R = 1$. These vector fields are shown in Figure 7. This illustrates an important advantage of using fuzzy spatial relations to guide the model, as a vector field can be defined towards the regions where the relations are more satisfied.

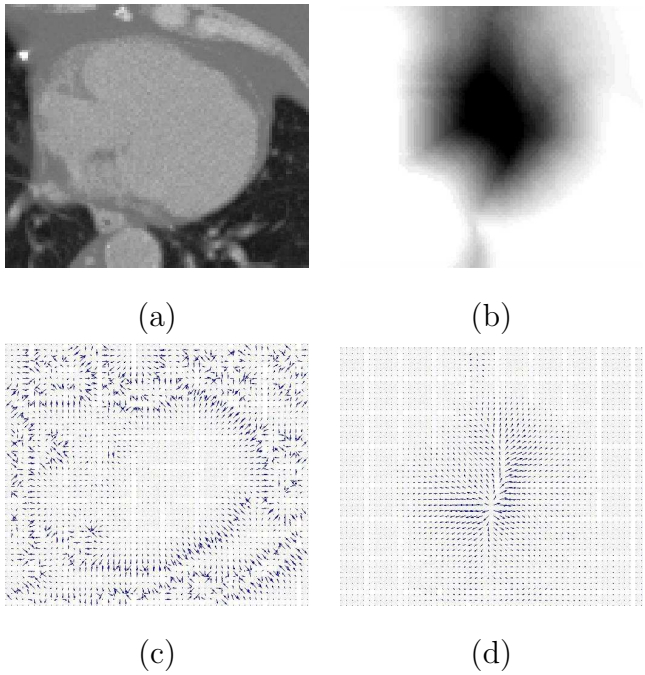

Fig. 7. Detail of the original CT image (a) and vector field $\mathbf{F}_{gvf}$ corresponding to the GVF (c). Detail of β_R (b) and vector field $\mathbf{F}_R$ associated (d).

Several methods for external forces that fulfill these properties are described in [39]. A gradient diffusion technique has been chosen due to the smoothness and the wide attraction range of the resulting vector field. Thus, the GVF is calculated by replacing the edge map of the original formulation with our fuzzy set β'_R:

$$\begin{cases} \frac{\partial \mathbf{u}}{\partial t} = c\nabla^2\mathbf{u} - ||\nabla\beta'_R||^2(\mathbf{u} - \nabla\beta'_R) \\ \mathbf{u}(x,0) = \nabla\beta'_R(x) \end{cases} \tag{11}$$

where t is the time parameter, x a point of space and c defines the trade-off between the two terms (here it is equal to 0.15 as suggested in [41]). The first equation is a combination of a diffusion term that will produce a smooth vector field and a data term that encourages $\mathbf{u}$ to stay close to $\nabla\beta'_R$, i.e. we want it to be stronger when the variations of β'_R are more important so that the deformable surface evolves from regions completely between the lungs towards regions not between the lungs. In regions where $||\nabla\beta'_R||$ is low, the diffusion term will prevail. The less the relation β'_R is satisfied the higher the modulus of the force should be, thus it has to be proportional to β_R. The following normalization is used: $\mathbf{F}_R = \beta_R \frac{\mathbf{u}}{||\mathbf{u}||}$ where $\mathbf{u}$ is the GVF defined by Equation 11.

4.3 Pressure force proportional to spatial relations

The term $\mathbf{F}_p$ in Equation 10 represents a pressure force [40], normal to the surface and which amplitude is $w_p(x) = k_1\,\beta_R + k_2$ where k_2 represents the modulus of a constant pressure in all points of space and k_1 weights a pressure term proportional to β_R. Their effect is explained in Section 5. This pressure force reinforces the effect of spatial relations and improves convergence as it is stronger at the points between the lungs which are the farthest from them (where β_R takes higher values), and it decreases when getting closer to them (where β_R takes lower values because the chosen spatial relations are less fulfilled). Indeed, this pressure force is needed to avoid the following effect: if the weight of $\mathbf{F}_R$ is increased only with respect to $\mathbf{F}_{gvf}$, the influence of the edge map is reduced and the accuracy of the segmentation near the contours of the image worsens.

5 Results

Our algorithm has been applied on 10 different cases of CT images. These exams come from different medical centers and have different characteristics

Radius of the initial sphere	Number of iterations	α	β	k_2	c
10 mm	10000	0.2	0.1	0.2	0.15 (0.05-0.3)

Table 2
Invariable parameters for all the cases in the database.

(size, resolution, contrast). Their sizes are $512 \times 512 \times Z$ voxels with Z varying from 63 to 122 and their resolutions are typically around 2 mm $\times$ 2 mm $\times$ dz mm for the three directions of the space (x, y and z respectively), with dz varying from 4.5 to 7.5 mm.

5.1 Parameter tuning

In our experiments, the following parameters have been used:

- The radius of the initial sphere for the deformable model is small enough (10 mm) to ensure that the starting surface is completely contained inside the contours of the heart. An example of the initial contour is shown in Figure 6.
- The value of λ is adapted for each particular case (see Table 3). In general, it gives a more important weight to the GVF force ($\mathbf{F}_{gvf}$) because it guides the deformable model towards the contours, whereas $\mathbf{F}_R$ represents a more general evolution. However, the spatial relation force remains necessary for the evolution of the deformable model as illustrated in Figure 8(a).
- The values of the constants k_1 and k_2 for the pressure force weight are shown in Tables 2 and 3. The parameter k_1 balances the pressure force in order to prevent the deformable model from inflating too much or too little and k_2 pushes softly the model in order to reach the contours of the heart far from the initial small sphere.
- The internal force coefficients in Equation 9 are $\alpha = 0.2$ and $\beta = 0.1$ which provide a good trade-off between tension and rigidity.
- The value of c in Equation 11 has been chosen equal to 0.15 because it is the classical value, as suggested in [41]. However, similar results are obtained for values of c between 0.05 and 0.3.

These parameters have been chosen empirically. Table 2 shows the values of the parameters that remain stable for all cases. Table 3 shows the values of the parameters to be adapted for different cases in order to obtain satisfactory results. λ may vary between 0.5 and 0.8 and k_1 has to be adapted depending on the case. The size of the dilation of the right lung (for K2) and the percentage of the bounding box of the lungs (used for K3) do not have to be changed in general, except for some particular cases (outliers of the distributions illus-

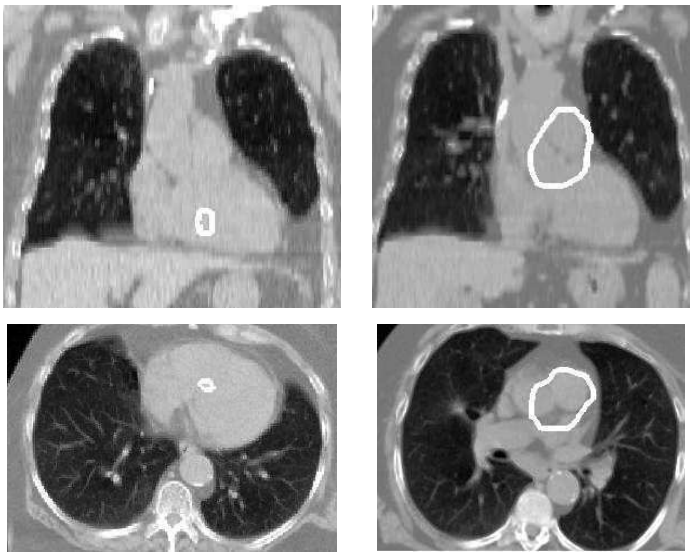

(a) (b)

Fig. 8. Coronal and axial views of some results of heart segmentation. The contours, superimposed on the CT image, have been calculated: (a) using only the GVF force, which is not sufficient at all; and (b) using the GVF and a pressure force weighted with the membership function of the spatial relations ($\mathbf{F}_p$), without the force derived directly from spatial relations. The result in (b) shows that $\mathbf{F}_R$ is fundamental for the segmentation of the heart as, without the force $\mathbf{F}_R$, the results are not satisfactory at all. These images correspond to the patient illustrated in Figure 5(a).

Patient	Dilation of right lung used for K2	% of bounding box of lungs used for K3	λ	k_1
1	3 cm	40 %	0.6	1
2	3 cm	33 %	0.7	1
3	3 cm	33 %	0.7	1
4	3 cm	25 %	0.6	0.1
5	3 cm	33 %	0.8	0.1
6	8 cm	33 %	0.7	2
7	3 cm	33 %	0.8	2
8	3 cm	25 %	0.7	2
9	3 cm	33 %	0.8	1
10	4 cm	33 %	0.5	2

Table 3
Parameters used for the patients in the database.

trated in Table 1).

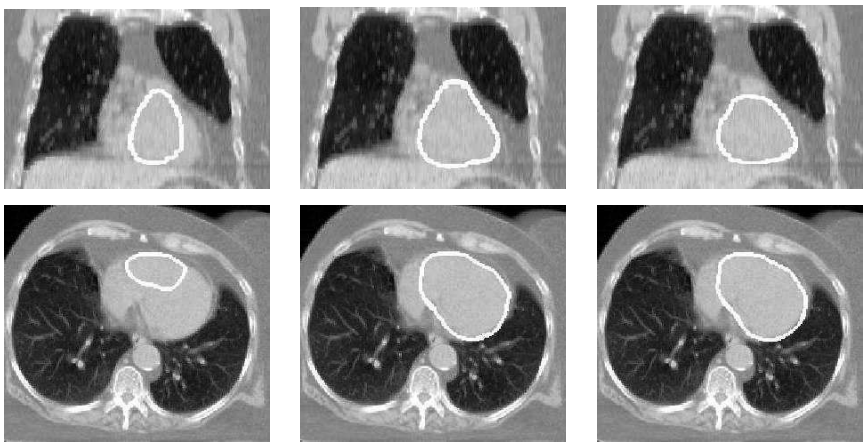

(a) (b) (c)

Fig. 9. Coronal (top row) and axial (bottom row) views of some results of heart segmentation. The contours, superimposed on the CT image, have been obtained: (a) using $\mathbf{F}_{gvf}$ and $\mathbf{F}_R$: the heart is not completely segmented; (b) adding a constant pressure force for the evolution of the deformable model: some parts of the aorta are included in the heart segmentation; (c) using $\mathbf{F}_{gvf}$, $\mathbf{F}_R$ and $\mathbf{F}_p$: this combination avoids the inclusion of other structures in the heart segmentation. These images correspond to the patient illustrated in Figure 5(a).

How to tune the parameters – The first parameters to fix are the distances for K2 and K3. This can be done by computing the sphere-ROI and the initial small sphere. If it is centered in the heart, it is a good initialization. Otherwise, the morphological dilation of the right lung should probably be increased. This stage could be realized by using a user interface in order to ease interaction. Then λ and k_1 have to be tuned. $\lambda = 0.7$ and $k_1 = 1$ are good initial parameters. Once the first result is computed, there exist several possibilities:

- If the resulting contour is too small compared with the heart or some parts of the organ (typically the apex) are not included in the segmentation, then k_1 (the pressure force) has to be increased.
- If the resulting segmentation is too large, then λ has to be increased in order to give more importance to the influence of the contours (the GVF) with respect to the spatial relations force.
- If the heart is correctly delineated but the segmentation includes some parts of the aorta or the liver, either λ has to be slightly increased or k_1 should be decreased a little.

These guidelines may be useful in cases the results are not completely satisfactory with the standard values of the parameters. However, in most cases,

these standard values lead to results that are accurate enough for radiotherapy purposes (since an additional security margin is added anyway).

Figures 8 and 9 show some results of the segmentation of the heart using different combinations of the forces:

- In Figure 9(a) the heart has been segmented using the GVF and a force derived from spatial relations. The GVF guides the model towards the contours of the images and $\mathbf{F}_R$ represents a more general evolution towards the regions not between the lungs as explained in Section 4. However, this combination is not sufficient to segment completely the heart since the deformable model does not reach the contours of the heart. For this reason, $\mathbf{F}_R$ must be reinforced with a pressure force if an under-segmentation of the heart is not desired.
- The addition of a constant pressure force for the evolution of the deformable model improves the result. Nevertheless, the model inflates with the same strength in all directions, including parts of the surrounding structures (the aorta, the mediastinum and the liver) in the heart segmentation (Figure 9(b)).
- The use of a pressure force weighted with the spatial relations avoids this undesired effect. This is illustrated in Figure 9(c) where a satisfactory result is obtained. In this case, we have used the GVF, a force derived from spatial relations and a pressure force weighted with the membership function of the spatial relations as in Equation 10. The addition of the spatial relations significantly improves the results. This is particularly visible near the left lung.
- If this weighted pressure force is used without the force directly derived from spatial relations, the results are not satisfactory at all, as it can be observed in Figure 8(b). In this case, the deformable model expands but, as the force of spatial relations is not present, the GVF guides the surface towards the strongest contours of the image and not towards the appropriate regions.

5.2 Computation time and complexity

The computation of the membership function "between the lungs" (K1) is the most expensive step with respect to computation time. The algorithm to compute the region "between" has a complexity in $O(n^2)$ where n is the number of voxels of the input image. However, the computation time is not a limitation (even in 3D) because the images can be under-sampled to obtain the region between the lungs, as a very precise result is not necessary at this stage. Thus, the image of the segmented lungs (with original sizes $512 \times 512 \times Z$ voxels with Z varying from 63 to 122) is under-sampled to a much lower size ($15 \times 15 \times 15$ voxels), the region between them is computed using Equation 1

Operation	Computer performances	Time
Total computation time under-sampling the images to $15 \times 15 \times 15$	Sun Sparc Ultra-4, 2 GB RAM	< 4 min
Total computation time without under-sampling the images: $512 \times 512 \times 63$	Sun Sparc Ultra-4, 2 GB RAM	~ 17 h

Table 4
Computation times for the membership function "between" the lungs without and with resampling of the images.

and finally the resulting image is resampled to the original size (using a linear interpolation). In these conditions, the total computation time is less than 4 minutes and the computation of the region between the lungs takes about 65% of the total time. However, without under-sampling the computation time is much higher as shown in Table 4. The manual segmentation of the heart can take about one hour for an expert. Therefore, the interest of the proposed method is to provide a fast result in a few minutes. Even if some interaction or even some correction of the result is necessary, our approach can ease the segmentation of the heart.

Noticeably, the important under-sampling of the images does not prevent obtaining a correct result. However, some parameters may have to be adapted. Figure 10 shows the results obtained without and with under-sampling and the optimal parameters for each case.

The number of iterations for the evolution of the deformable model is set to 10000, which has been empirically proven to be sufficient for convergence of the model, as the same results are obtained with a higher number of iterations. This takes less than 1 minute with a 3.2 GHz (Pentium 4) Intel CPU, 1 GB RAM.

5.3 Evaluation

In Figure 11 the results of our automatic heart segmentation method (in white) are compared with the manual segmentations (in black) for patients in Figures 5(b-e). It can be observed that even for an expert the delineation of the limits of the heart in these regions remains very challenging due to the low contrast of the images. The further application of our segmentation algorithm is radiotherapy planning, where a large margin is outlined around the pathologies to irradiate. Therefore, the results illustrated here are considered as satisfactory.

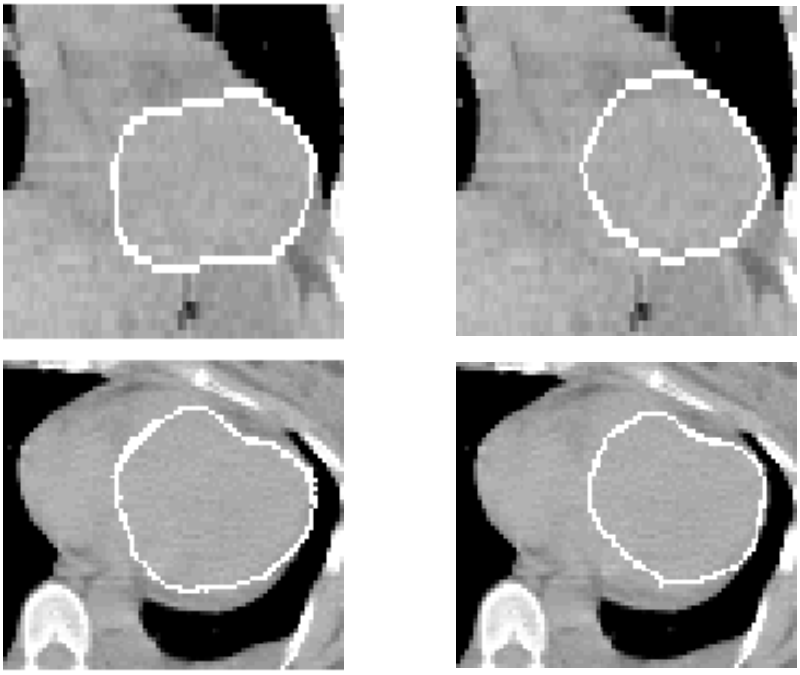

Resampling: $15 \times 15 \times 15$ No resampling: $512 \times 512 \times 63$

$\lambda = 0.6$; $k_1 = 0.1$ $\lambda = 0.5$; $k_1 = 2$

Fig. 10. Detail of the results of the segmentation of the heart for patient 4 with and without resampling and the adapted parameters.

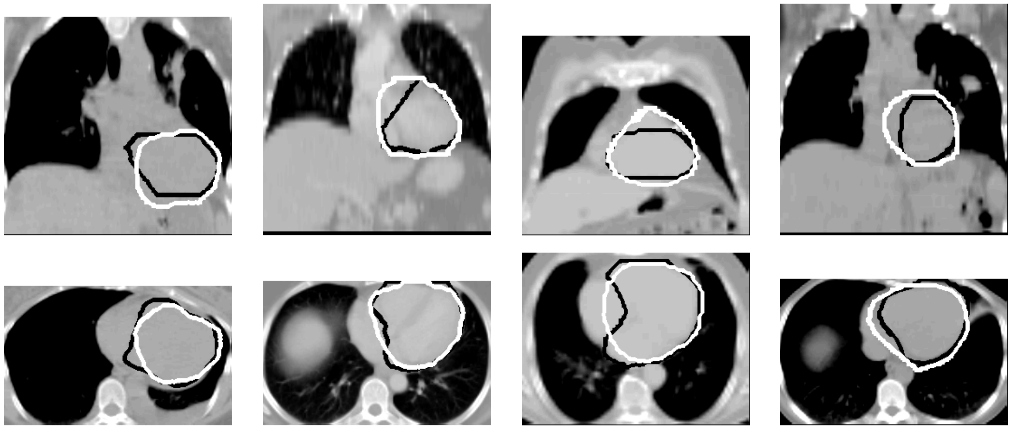

(a) (b) (c) (d)

Fig. 11. Manual (black) and automatic (white) segmentations of the heart using our method for patients illustrated in Figures 5(b-e).

In order to evaluate quantitatively our results, the 10 automatic segmentations obtained with our algorithm (A) have been compared with the 10 corresponding manual segmentations furnished by an expert (M). In the following $|A|$ is the cardinality of the set of voxels A. Results are quantitatively assessed using different criteria:

- the similarity index $S = \frac{2|M \cap A|}{|M|+|A|}$ [42],
- the sensitivity $SENS(M, A) = \frac{|M \cap A|}{|M|}$,
- the specificity $SPEC(M, A) = \frac{|M \cap A|}{|A|}$ between both volumes,
- the mean distance $D_m(M, A) = \frac{1}{2}[d_m(M, A) + d_m(A, M)]$
  with $d_m(M, A) = \frac{1}{|M|} \sum_{p \in M} \min_{q \in A} d(p, q)$,
  where d is the Euclidean distance, between the surfaces.

As explained in [42] the similarity index S is sensitive to variations in shape, size and position and a value of $S > 0.7$ indicates a strong agreement. The value of S is equal to 1 when A and M totally overlap. The sensitivity ($SENS$) and specificity ($SPEC$) measures give us additional information about how the overlap of both structures is achieved. For instance, if the comparison of A and M yields a low sensitivity value but a high specificity one, it means that the automatic segmentation is too small. Both criteria are also equal to 1 if total overlap is achieved.

5.4 Discussion

Table 5 shows the obtained results. It can be observed that results are satisfactory as S is higher than 0.7 for almost all 10 cases. This is also confirmed by the high values of sensitivity and specificity. As stated above, the voxel resolutions in Z of these CT exams varies from 4.5 to 7.5 mm. Therefore, mean distances from 3.9 to 9.3 mm are perfectly acceptable. These results are also satisfactory if they are compared with the 5.5 mm of average error obtained by Funka-Lea et al. in [13] on contrast CT exams with sub-millimeter resolutions.

It can be observed that the values of the specificity are in general lower than those of the sensitivity. This means that our method furnishes segmentations of the heart larger than the manual delineations, which is consistent with the fact that, in radiotherapy applications, larger results are preferred to under-segmentations (see examples in Figures 11(b), (c) and (d) corresponding to patients 5, 2 and 1 respectively).

The best results are obtained for patient 4, illustrated in Figure 11(a). Indeed, the result of the automatic segmentation is visually close to the manual one. This is confirmed by the high value of S (0.84) and the low mean distance (3.9 mm). Sensitivity and specificity have high values (0.83 and 0.84 respectively) in this case.

The highest mean distance is the one of patient 2. In this case, the segmentation includes a part of the aorta (see Figure 11(c)). This is due to the fact that there is no edge information to separate it from the heart. This is one

Patient	Similarity index	Sensitivity	Specificity	Mean distance
1	0.77	0.96	0.64	6.4
2	0.70	0.90	0.58	9.3
3	0.74	0.92	0.62	7.4
4	0.84	0.83	0.84	3.9
5	0.80	0.91	0.71	4.9
6 (3 cm)	0.57	0.46	0.40	11.2
6 (8 cm)	0.75	0.78	0.72	6.1
7	0.71	0.88	0.60	6.6
8	0.67	0.71	0.62	7.1
9	0.77	0.81	0.73	4.5
10	0.64	0.60	0.70	7.8

Table 5
Results of comparing the manual segmentations of the heart with the results obtained with our automatic method for different patient images. Distance are in millimeters (mm).

of the most challenging difficulties of our approach. Another difficulty is the separation of the heart and the liver. However, our method furnishes correct results for all cases. Only for patient 4 (Figure 11(a)) a small part of the liver has been included in the heart segmentation.

Two different results are shown for patient 6 in Table 5. For one of them a morphological dilation of 3 cm was performed for K2, and for the other one the dilation was of 8 cm. The low values of the similarity index, sensitivity and specificity, and the high mean distance, show that the segmentation was not correct with 3 cm. The used parameters furnished a wrong initialization (the small sphere was not centered in the heart). Therefore, based on visual inspection of the images, this was corrected by using a dilation of 8 cm and results have been notably improved.

Our algorithm has been used on images coming from different centers and from different patients. Thus, there are differences in the contrast of the images and in the anatomy of the patients. Due to the differences in contrast, some limits between organs (or inside them) are visible in some of the studies and not in others. For example, a quite clear contour can be seen inside the heart in Figure 11(b), which is not present in the other cases. Our automatic segmentation approach deals with these differences. However, as illustrated with patient 6, the variations in anatomy from one patient to another are sometimes important and thus some parameters have to be adjusted for different images. In

particular, in exams realized on children or in the case of lung resection, the parameters (and specially those based on distances) will probably need to be tuned. This may happen with different CT acquisition protocols, i.e. images acquired during normal breathing or in maximal inspiration (in this work the CT images are acquired in maximal inspiration). All the distances could be normalized with respect to the size of the lungs or to the size of the body, in order to find the parameters that could fit in all cases.

6 Conclusion

We propose an approach that uses fuzzy structural knowledge coming from spatial relations in order to segment the heart in CT images in a robust way. First, spatial relations are used to define the region of interest of the heart and then, from the fuzzy sets representing the spatial relations, a new external force is derived and it is introduced in the evolution scheme of a deformable model.

As illustrated by our results, the modeling of the spatial relations and their incorporation into the deformable model evolution significantly improve the segmentation of the heart compared with the classical approaches that are guided by a pressure force and GVF, by excluding non-desirable structures such as the aorta or the liver. The results have been evaluated by comparing them with segmentations of the heart realized manually by an expert, which shows the accuracy attained with our approach. These preliminary quantitative results show a strong agreement between the manual segmentations and the ones obtained by our approach, and confirm the potential of the proposed method. Nevertheless, the segmentation of the heart in CT images remains a difficult task as, even for experts, it is complicated to define the limits of this organ in this modality. For this reason, our method should be applied to larger databases, with manual segmentations obtained from a common agreement of a group of experts to go further in the evaluation.

One of the foreseen applications of our method is radiotherapy planning. Usually radiotherapists delineate a relatively wide margin around sensitive organs which must not be affected by radiation. This margin, which may be of several centimeters (particularly in the lungs due to the breathing) is much larger than the mean distances shown in Table 5. Thus, the obtained results show that our segmentation method provides accurate enough results for the segmentation of the heart. Figure 12 shows some results of heart segmentation with a tumor in the lungs. This illustrates the usefulness of the segmentation of the heart in radiotherapy planning as, once the segmentations of the heart and the tumor are computed, the delineation of the security margins are much easier and could even be automated. In addition to this, our method can also

be used for diagnosis of other cardiovascular diseases. In particular, the new combined devices PET/CT and SPECT/CT, widely used in cardiology and oncology, often furnish non-contrast and low-resolution CT images. Our approach, as opposed to the one by Funka-Lea et al. [13] for example, is adapted to this type of data.

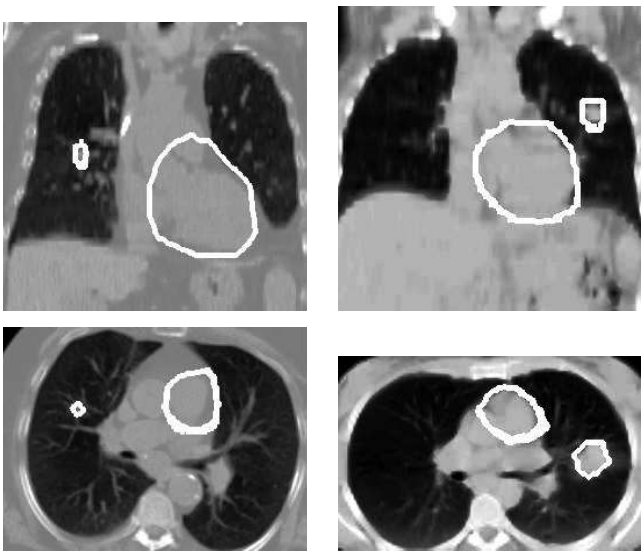

(a) (b)

Fig. 12. Results of automatic heart segmentation for two cases where a tumor is present in the right (a) and in the left lung (b). Images in (a) correspond to the patient illustrated in Figure 5(a) and images in (b) to the patient in Figure 5(e).

Future work aims at applying our algorithm to other imaging modalities such as positron emission tomography (PET) images, and experimenting with other definitions of the spatial relation "between" [26]. In addition to this, the research of the best parameter combination could be automated in order to take into account potential variations in anatomy. The most sensitive step of our method is the initialization of the deformable model. If the small sphere is not centered inside the heart, the results of the segmentation may be unsatisfactory. This step can be improved by adding an interactive interface at this stage in order to let the user correct the initialization if necessary. This kind of interaction is easily accepted and even often desired by clinicians.

Further applications include the use of the segmentation of the heart in registration algorithms based on structures [43] or based on features/landmarks [44], necessary even in PET/CT and SPECT/CT combined devices, and subsequently, in radiotherapy planning procedures.

Acknowledgements

The authors would like to thank Liège, Lille, Louisville and Val de Grâce Hospitals for the images and the members of Segami Corporation for their contribution to this project. This work was partially supported by the French Ministry of Research, by the CAPES (BEX3402/04-5) and by a "ParisTech/Région Ile-de-France" Fellowship.

References

[1] T. McInerney, D. Terzopoulos, A Dynamic Finite Element Surface Model for Segmentation and Tracking in Multidimensional Medical Images with Application to Cardiac 4D Image Analysis, Computerized Medical Imaging and Graphics 19 (1) (1995) 69–83.

[2] J. S. Suri, Computer Vision, Pattern Recognition and Image Processing in Left Ventricle Segmentation: The Last 50 Years, Pattern Analysis & Applications 3 (3) (2000) 209–242.

[3] H. Assen, M. Danilouchkine, A. Frangi, S. Ordás, J. Westenberg, J. Reiber, B. Lelieveldt, SPASM: A 3D-ASM for Segmentation of Sparse and Arbitrarily Oriented Cardiac MRI Data, Medical Image Analysis 10 (2) (2006) 286–303.

[4] L. Zhukov, Z. Bao, I. Guskov, J. Wood, D. Breen, Dynamic Deformable Models for 3D MRI Heart Segmentation, in: SPIE Medical Imaging, Vol. 4684, San Diego, California, USA, 2002, pp. 1398–1405.

[5] N. Noble, D. Hill, M. Breeuwer, J. Schnabel, D. Hawkes, F. Gerritsen, R. Razavi, Myocardial Delineation Via Registration in a Polar Coordinate System, in: 5th International Conference on Medical Image Computing and Computer-Assisted Intervention (MICCAI), Part I, Vol. 2488 of Lecture Notes in Computer Science (LNCS), Springer-Verlag Berlin / Heidelberg, Tokyo, Japan, 2002, pp. 651–658.

[6] C. Tauber, H. Batatia, A. Ayache, Contours Actifs Basés sur Trois Energies : Détection des Cavités Cardiaques, in: 15^e Congrès Francophone AFRIF-AFIA Reconnaissance des Formes et Intelligence Artificielle (RFIA'2006), Tours, France, 2006.

[7] M. Lynch, O. Ghita, P. Whelan, Automatic Segmentation of the Left Ventricle Cavity and Myocardium in MRI Data, Computers in Biology and Medicine 36 (4) (2006) 389–407.

[8] P. H. Gregson, Automatic Segmentation of the Heart in 3D MR Images, in: Canadian Conference on Electrical and Computer Engineering, Vol. 2, 1994, pp. 584–587.

[9] B. P. F. Lelieveldt, R. J. van der Geest, M. R. Rezaee, J. G. Bosch, J. H. C. Reiber, Anatomical Model Matching with Fuzzy Implicit Surfaces for Segmentation of Thoracic Volume Scans, IEEE Transactions on Medical Imaging 18 (3) (1999) 218–230.

[10] M. Kaus, J. von Berg, W. Niessen, V. Pekar, Automated Segmentation of the Left Ventricle in Cardiac MRI, in: International Conference on Medical Image Computing and Computer-Assisted Intervention (MICCAI), Vol. 2878 of Lecture Notes in Computer Science (LNCS), Springer-Verlag, 2003, pp. 432–439.

[11] C. Pluempitiwiriyawej, J. Moura, Y. Wu, C. Ho, STACS: New Active Contour Scheme for Cardiac MR Image Segmentation, IEEE Transactions on Medical Imaging 24 (5) (2005) 593–603.

[12] B. Pfeifer, F. Hanser, T. Trieb, C. Hintermüller, M. Seger, G. Fischer, R. Modre, B. Tilg, Combining Active Appearance Models and Morphological Operators Using a Pipeline for Automatic Myocardium Extraction, in: Functional Imaging and Modeling of the Heart (FIMH), Third International Workshop, Vol. 3504 of Lecture Notes in Computer Science (LNCS), Barcelona, Spain, 2005, pp. 44–53.

[13] G. Funka-Lea, Y. Boykov, C. Florin, M.-P. Jolly, R. Moreau-Gobard, R. Ramaraj, D. Rinck, Automatic Heart Isolation for CT Coronary Visualization Using Graph-Cuts, in: IEEE International Symposium on Biomedical Imaging (ISBI), Arlington, Virginia, USA, 2006, pp. 614–617.

[14] M. Jolly, Automatic Segmentation of the Left Ventricle in Cardiac MR and CT Images, International Journal of Computer Vision 70 (2) (2006) 151–163.

[15] O. Ecabert, J. Peters, C. Lorenz, J. von Berg, M. Vembar, K. Subramanyan, G. Lavi, J. Weese, Towards Automatic Full Heart Segmentation in Computed-Tomography Images, in: Computers in Cardiology, Vol. 32, Lyon, France, 2005, pp. 223–226.

[16] O. Ecabert, J. Peters, M. Walker, J. Berg, C. Lorenz, M. Vembar, M. Olszewski, J. Weese, Automatic Whole Heart Segmentation in CT Images: Method and Validation, in: J. Pluim, J. Reinhardt (Eds.), SPIE Medical Imaging, Vol. 6512, San Diego, California, USA, 2007.

[17] Y. Boykov, G. Funka-Lea, Graph Cuts and Efficient N-D Image Segmentation, International Journal of Computer Vision 70 (2) (2006) 109–131.

[18] O. Juan, Y. Boykov, Active Graph Cuts, in: IEEE Computer Society Conference on Computer Vision and Pattern Recognition, Vol. 1, Los Alamitos, California, USA, 2006, pp. 1023–1029.

[19] O. Colliot, O. Camara, R. Dewynter, I. Bloch, Description of Brain Internal Structures by Means of Spatial Relations for MR Image Segmentation, in: SPIE Medical Imaging, Vol. 5370, San Diego, California, USA, 2004, pp. 444–455.

[20] O. Camara, O. Colliot, I. Bloch, Computational Modeling of Thoracic and Abdominal Anatomy Using Spatial Relationships for Image Segmentation, Real-Time Imaging 10 (4) (2004) 263–273.

[21] J. Atif, C. Hudelot, G. Fouquier, I. Bloch, E. Angelini, From Generic Knowledge to Specific Reasoning for Medical Image Interpretation Using Graph-Based Representations, in: International Joint Conference on Artificial Intelligence (IJCAI), Hyderabad, India, 2007, pp. 224–229.

[22] H. Khotanlou, J. Atif, E. Angelini, H. Duffau, I. Bloch, Adaptive Segmentation of Internal Brain Structures in Pathological MR Images Depending on Tumor Types, in: IEEE International Symposium on Biomedical Imaging (ISBI), Washington DC, USA, 2007, to appear.

[23] J. Yang, L. Staib, J. Duncan, Neighbor-Constrained Segmentation with Level Set Based 3-D Deformable Models, IEEE Transactions on Medical Imaging 23 (8) (2004) 940–948.

[24] A. Moreno, C. Takemura, O. Colliot, O. Camara, I. Bloch, Heart Segmentation in Medical Images Using the Fuzzy Spatial Relation "Between", in: Information Processing and Management of Uncertainty in Knowledge-Based Systems (IPMU), Paris, France, 2006, pp. 2052–2059.

[25] C. Xu, J. Prince, Gradient Vector Flow: A New External Force for Snakes, in: IEEE Computer Society Conference on Computer Vision and Pattern Recognition, Los Alamitos, San Juan, Puerto Rico, 1997, pp. 66–71.

[26] I. Bloch, O. Colliot, R. Cesar, On the Ternary Spatial Relation "Between", IEEE Transactions on Systems, Man, and Cybernetics SMC-B 36 (2) (2006) 312–327.

[27] I. Bloch, H. Maître, Fuzzy Mathematical Morphologies: A Comparative Study, Pattern Recognition 28 (9) (1995) 1341–1387.

[28] K. Miyajima, A. Ralescu, Spatial Organization in 2D Segmented Images: Representation and Recognition of Primitive Spatial Relations, Fuzzy Sets and Systems 65 (2/3) (1994) 225–236.

[29] I. Bloch, A. Ralescu, Directional Relative Position between Objects in Image Processing: A Comparison between Fuzzy Approaches, Pattern Recognition 36 (2003) 1563–1582.

[30] I. Bloch, Fuzzy Relative Position between Objects in Image Processing: a Morphological Approach, IEEE Transactions on Pattern Analysis and Machine Intelligence 21 (7) (1999) 657–664.

[31] G. Borgefors, Distance Transformations in Digital Images, Computer Vision, Graphics, and Image Processing (CVGIP) 34 (3) (1986) 344–371.

[32] M. Kass, A. Witkin, D. Terzopoulos, Snakes: Active Contour Models, International Journal of Computer Vision 1 (4) (1987) 321–331.

[33] T. McInerney, D. Terzopoulos, Deformable Models in Medical Image Analysis: A Survey, Medical Image Analysis 1 (2) (1996) 91–108.

[34] C. Xu, J. Prince, Handbook of Medical Imaging, Ed. Isaac Bankman, Academic Press, 2000, Ch. Gradient Vector Flow Deformable Models, pp. 159–169.

[35] J. Montagnat, H. Delingette, N. Scapel, N. Ayache, Representation, Shape, Topology and Evolution of Deformable Surfaces. Application to 3D Medical Image Segmentation, Tech. rep., Institut National de Recherche en Informatique et en Automatique (INRIA), Sophia Antipolis, France, iSRN INRIA/RR–3954–FR+ENG (may 2000).

[36] U. Meier, O. López, C. Monserrat, M. Juan, M. Alcañiz, Real-Time Deformable Models for Surgery Simulation: A Survey, Computer Methods and Programs in Biomedicine 77 (3) (2005) 183–197.

[37] J. Liang, T. McInerney, D. Terzopoulos, United Snakes, Medical Image Analysis 10 (2) (2006) 215–233.

[38] O. Colliot, O. Camara, I. Bloch, Integration of Fuzzy Spatial Relations in Deformable Models - Application to Brain MRI Segmentation, Pattern Recognition 39 (8) (2006) 1401–1414.

[39] O. Colliot, O. Camara, I. Bloch, Integration of Fuzzy Structural Information in Deformable Models, in: Information Processing and Management of Uncertainty in Knowledge-Based Systems (IPMU), Vol. 2, Perugia, Italy, 2004, pp. 1533–1540.

[40] L. Cohen, On Active Contour Models and Balloons, Computer Vision, Graphics, and Image Processing: Image Understanding (CVGIP:IU) 53 (2) (1991) 211–218.

[41] C. Xu, J. Prince, Snakes, Shapes, and Gradient Vector Flow, IEEE Transactions on Medical Imaging 7 (3) (1998) 359–369.

[42] A. Zijdenbos, B. Dawant, R. Margolin, A. Palmer, Morphometric Analysis of White Matter Lesions in MR Images: Method and Validation, IEEE Transactions on Medical Imaging 13 (4) (1994) 716–724.

[43] O. Camara, G. Delso, O. Colliot, A. Moreno-Ingelmo, I. Bloch, Explicit Incorporation of Prior Anatomical Information into a Nonrigid Registration of Thoracic and Abdominal CT and 18-FDG Whole-Body Emision PET Images, IEEE Transactions on Medical Imaging 26 (2) (2007) 164–178.

[44] S. Chambon, A. Moreno, A. Santhanam, J. Rolland, E. Angelini, I. Bloch, CT-PET Landmark-based Registration using a Dynamic Lung Model, in: International Conference on Image Analysis and Processing (ICIAP), Modena, Italy, 2007.